ADVANCED HEALTHCARE MATERIALS
www.advhealthmat.de

A Strategy of Fenton Reaction Cycloacceleration for High-Performance Ferroptosis Therapy Initiated by Tumor Microenvironment Remodeling

Lin Huang, Jie Feng, Jiaoyang Zhu, Jing Yang, Wei Xiong, Xuanyi Lu, Sijin Chen, Sugeun Yang, Yan Li, Yikai Xu,* and Zheyu Shen**

The emerging tumor ferroptosis therapy confronts impediments of the tumor microenvironment (TME) with weak intrinsic acidity, inadequate endogenous H_2O_2, and a powerful intracellular redox balance system that eliminates toxic reactive oxygen species (ROS). Herein, a strategy of Fenton reaction cycloacceleration initiated by remodeling the TME for magnetic resonance imaging (MRI)-guided high-performance ferroptosis therapy of tumors is proposed. The synthesized nanocomplex exhibits enhanced accumulation at carbonic anhydrase IX (CAIX)-positive tumors based on the CAIX-mediated active targeting, and increased acidification via the inhibition of CAIX by 4-(2-aminoethyl) benzene sulfonamide (ABS) (remodeling TME). This accumulated H^+ and abundant glutathione in TME synergistically trigger biodegradation of the nanocomplex to release the loaded cuprous oxide nanodots (CON), β-lapachon (LAP), Fe^{3+}, and gallic acid-ferric ions coordination networks (GF). The Fenton and Fenton-like reactions are cycloaccelerated via the catalytic loop of Fe-Cu, and the LAP-triggered and nicotinamide adenine dinucleotide phosphate quinone oxidoreductase1-mediated redox cycle, generating robust ROS and plenitudinous lipid peroxides accumulation for ferroptosis of tumor cells. The detached GF network has improved relaxivities in response to the TME. Therefore, the strategy of Fenton reaction cycloacceleration initiated by remodeling the TME is promising for MRI-guided high-performance ferroptosis therapy of tumors.

1. Introduction

Ferroptosis therapy is an emerging iron-dependent modality of antitumor, which utilizes Fenton or Fenton-like catalytic reactions between metal ions (e.g., Fe^{2+}, Cu^{2+}, Mn^{2+}, or Co^{4+}) and hydrogen peroxide (H_2O_2) to generate highly cytotoxic oxidative hydroxyl radicals (•OH), thus resulting in cell death induced by the overload of lipid peroxides (LPO) on cellular membranes.[1] Unfortunately, the Fenton/Fenton-like catalytic activities are confined by the inherently insufficient H_2O_2 concentration in the tumor microenvironment (TME), resulting in poor efficacy of ferroptosis therapy.[2] Importantly, the presence of a strong intracellular defense system (i.e., the excessively produced reactive oxygen species (ROS) can be eliminated by the oversaturated reductive glutathione (GSH) in tumor cells to persevere the intracellular redox balance)[3] also causes the poor efficiency of ferroptosis therapy.

To overcome the above limitations of tumor ferroptosis therapy, abundant nanomedicines with capability of TME remolding or excellent catalytic performance at physiological condition have been developed for enhancing ferroptosis of tumor cells.[4] For instance, Dong et al. developed a novel perfluorocarbon @manganese oxide (MnO_x) core–shell nanoparticles with capability of ample ROS production and GSH consumption for boosting the ferroptosis-based anticancer treatment.[5] Yue et al. constructed the adenosine triphosphate (ATP) and acidity co-activated catalysis nanoplatforms with increased cellular H_2O_2 for efficient ferroptosis-based therapy.[6] Guan et al. designed a microenvironment-responsive nanoplatform (R-PtWMn) with high catalytic activity, leading to the enhanced ferroptosis of tumor by augmenting ROS yield and eliminating excess GSH.[3b] Chang et al. reported a single-atom Pd

---

L. Huang, J. Zhu, J. Yang, X. Lu, Y. Li, Z. Shen
School of Biomedical Engineering
Southern Medical University
1023 Shatai South Road, Guangzhou, Guangdong 510515, China
E-mail: sz@smu.edu.cn

The ORCID identification number(s) for the author(s) of this article can be found under https://doi.org/10.1002/adhm.202203362

DOI: 10.1002/adhm.202203362

J. Feng, W. Xiong, S. Chen, Y. Xu
Medical Imaging Center
Nanfang Hospital
Southern Medical University
1023 Shatai South Road, Guangzhou, Guangdong 510515, China
E-mail: fjnfyy@smu.edu.cn; yikai@smu.edu.cn

S. Yang
Department of Biomedical Science
BK21 FOUR Program in Biomedical Science and Engineering
Inha University College of Medicine
Incheon 22212, South Korea

nanozyme with dual peroxidase and GSH oxidase mimicking activities for promoting ferroptosis-based anticancer therapy.[7] The improvement of ferroptosis therapy efficiency by these strategies is significant, but still limited due to the relatively slow rate of Fenton reaction.

Because the conversion from Fe^{3+} to Fe^{2+} as depicted in Equation (1) is ineffective due to the low k_1 (0.0026 M^{-1} s^{-1}), the ROS generation is dominated by Fe^{2+}-mediated catalysis (k_2 = 570 M^{-1} s^{-1}) as depicted in Equation (2). The yield of ROS via Fenton reaction is restricted owing to the almost invalid Fe^{3+}/Fe^{2+} catalytic loop.[8] The Cu^+-assisted Fenton reaction system as depicted in Equation (3) has been confirmed. The efficient transition of Fe/Cu valence can be used as a powerful catalytic loop, and then reinforces the efficacy of ROS generation. Koo et al. reported a 3-nm-sized copper-iron peroxide nanocatalyzers to meliorate tumor therapeutic efficacy via a cooperative Fenton reaction of Fe^{3+} and Cu^+ rather than their standalone actions, which can respond to the acidic TME, achieve self-supply of H_2O_2, and subsequently facilitate the catalytic loop of Fe–Cu.[9] Nevertheless, the weak intrinsic acidity (pH 6.7–6.8) in the TME cannot fully implement the ferroptosis therapy utilizing the above nanocatalyzers, and another main obstacle is the "off-target" delivery that causes the non-selective Fenton reaction to normal tissues and cells. Therefore, innovative strategies are still needed to improve the outcomes of tumor ferroptosis therapy.

$$\mathrm{Fe}^3 + +\mathrm{H}_2\mathrm{O}_2 \rightarrow \mathrm{Fe}^{2+} + \mathrm{HO}_2 \cdot +\mathrm{H}^+ \qquad k_1 = 0.0026\,\mathrm{M}^{-1}\mathrm{s}^{-}1 \quad (1)$$

$$\mathrm{Fe}^{2+} + \mathrm{H}_2\mathrm{O}_2 \rightarrow \mathrm{Fe}^3 + + \cdot \mathrm{OH} + \mathrm{OH}^- \qquad k_2 = 570\,\mathrm{M}^{-1}\mathrm{S}^{-1} \quad (2)$$

$$\mathrm{Cu}^+ + \mathrm{Fe}^3 + \rightarrow \mathrm{Cu}^2 + +\mathrm{Fe}^2 + \qquad \Delta E^0 = 0.6\ \mathrm{V} \quad (3)$$

In this study, we innovatively propose a strategy of high-performance ferroptosis therapy of tumors based on Fenton reaction cycloacceleration initiated by regulating TME. Typically, the hollow core of hollow mesoporous organosilica nanoparticles (HMON) is utilized as a nanoreactor for "in situ cuprous oxide nanodots (CON) growth" to synthesize CON-loaded HMON (CON-HMON) via a hydrazine reduction method. After that, β-lapachon (LAP), a H_2O_2 donor based on the nicotinamide adenine dinucleotide phosphate (NADPH) quinone oxidoreductase1 (NQO1)-mediated redox cycle,[10] is encapsulated into the pore channel of CON-HMON, and the gallic acid-ferric ions (GF) coordination networks are deposited on the nanoparticle surface to prepare CON-LAP-HMON@GF, which is capable of preventing the premature leakage of CON and LAP from HMON. A carbonic anhydrase IX (CAIX) inhibitor (4-(2-aminoethyl) benzene sulfonamide, ABS) and polyethylene glycol (PEG) are further conjugated onto the nanoparticle surface via amidation reaction, generating CON-LAP-HMON@GF-ABS-PEG nanocomplex (**Scheme 1**a). The fabricated CON-LAP-HMON@GF-ABS-PEG can accumulate in CAIX-positive tumors due to the enhanced permeability and retention (EPR) effect (i.e., passive targeting), and then be efficiently internalized into the CAIX-positive cancer cells because of the high affinity between ABS linked in nanocomplex and CAIX (i.e., active targeting). The ABS can inactivate the CAIX enzyme, and thus increase the extracellular and intracellular H^+, establishing more acidic TME. After degradation of HMON by the accumulated H^+ and abundant GSH in TME, the CON, LAP, Fe^{3+}, and GF could be released. The CON can react with the increased extracellular and intracellular H^+, generating Cu^+. The Fe^{3+} reacts with Cu^+, producing Fe^{2+} and Cu^{2+} to accelerate the Fenton and Fenton-like reactions. The released LAP can produce H_2O_2 via the NQO1-mediated redox cycle (i.e., remodeling TME) to further accelerate the Fenton and Fenton-like reactions. Overall, the cycloacceleration of Fenton and Fenton-like reactions initiated by regulating TME can generate robust ROS for high-performance ferroptosis therapy of tumors. Meanwhile, the T_1-weighted magnetic resonance imaging (MRI) signals of the GF networks, which are TME-responsively detached from HMON, allows for monitoring of the progress of tumor ferroptosis therapy (Scheme 1b).

2. Results and Discussion

2.1. Synthesis and Characterizations of the CON-LAP-HMON@GF-ABS-PEG

HMON was synthesized based on a reported "chemical homology" mechanism,[11] where the mesoporous SiO_2 nanoparticles (MSN) acted as the hard template for the coating of a MON layer (denoted as MSN@MON). The inner MSN core was selectively etched away using hot ammonia, thus yielding tetrasulfide-bridged HMON. Then, the hollow core of HMON was utilized as a nanoreactor for "in situ CON growth" to prepare CON-HMON by hydrazine reduction method under nitrogen atmosphere. CON1-4-HMON is prepared sequentially by adjusting the feeding concentration of Cu (2.5–20 mm). The synthesis conditions and characterization results of the CON1-4-HMON are summarized in Table S1, Supporting Information. TEM images of CON1-3-HMON show that the CON formed in situ in the core gradually fills the entire hollow cores of HMON with the augment of the feeding Cu^{2+} concentration (Figure S1a–c, Supporting Information), whereas large amounts of CON away from HMON are observed in CON4-HMON sample due to too high feeding Cu^{2+} concentration (Figure S1d, Supporting Information). After storage at room temperature for 3 days, CON1-3-HMON is dispersed well in water, but CON4-HMON precipitates. That's because CON1-3-HMON are highly negatively charged resulting in strong electrostatic repulsion between nanoparticles, but CON4-HMON is slightly positively charged (average zeta potential = 3.1 ± 0.7 mV) due to the overloading of CON leading to very weak electrostatic repulsion between nanoparticles and aggregation of nanoparticles (Figure S2a,b, Supporting Information). Thus, CON3-HMON is chosen as the optimal sample for the next step of synthesis due to its high Cu loading content (13.8%) determined by inductively coupled plasma optical emission spectrometry (ICP-OES).

The reaction between Cu^+ and Fe^{3+}[9] as shown in the Equation (3) and Scheme 1b is beneficial to accelerate the Fenton reaction rate and generate robust •OH. Thus, in this study, the Fe^{3+} is chelated with gallic acid, forming gallic acid-ferric ions (GF) coordination networks deposited on the surface of CON3-HMON. CON3-HMON@GF1-8 is prepared sequentially by adjusting the feeding concentration of Fe and GA. The synthesis conditions and characterization results of the CON3-HMON@GF1-8 are summarized in Table S2, Supporting Information. Considering the loading content of total metal ions,

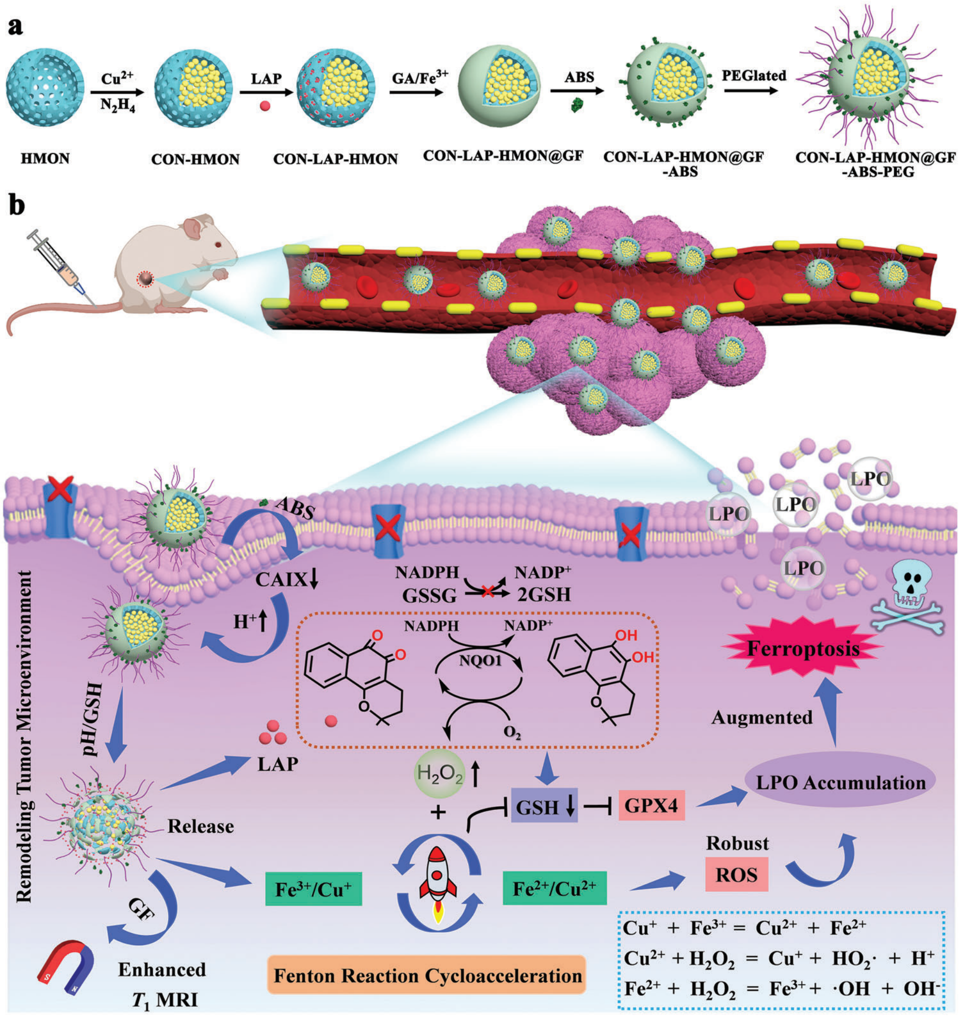

Scheme 1. a) Schematic illustration for the construction of CON-LAP-HMON@GF-ABS-PEG nanocomplex. b) Schematic illustration of high-performance ferroptosis therapy of tumors based on a strategy of Fenton reaction cycloacceleration initiated by regulating tumor microenvironment.

the resulting CON3-HMON@GF7 was chosen as the optimal one for the subsequent procedures.

Since HMON is also an excellent drug delivery vehicle, the LAP was encapsulated within the mesoporous channels of CON3-HMON before modification of GF coordination networks on the surface to prevent the leakage of CON and LAP, followed by modification of ABS and PEG via amidation reaction to obtain the final CON3-LAP-HMON@GF7-ABS-PEG nanocomplex. According to the UV–vis spectra (Figure S3a–c, Supporting Information), the loading content of LAP is calculated to be 4.6% for CON3-LAP-HMON@GF7-ABS-PEG. Figure S4, Supporting Information, shows the Fourier transform infrared spectroscopy (FTIR) of HMON, CON3-LAP-HMON@GF7, ABS, CON3-LAP-HMON@GF7-ABS, and CON3-LAP-HMON@GF7-ABS-PEG. Specifically, CON3-LAP-HMON@GF7 shows two characteristic peaks at 1396 and 1296 cm^{-1}, which correspond to LAP. The peak at 1537 cm^{-1} assigns to the stretching vibration of N–H in C–NH_2 of ABS. The CON3-LAP-HMON@GF7-ABS exhibits two new peaks at 1650 cm^{-1} corresponding to amide bond, which indicates the successful grafting of ABS by the amidation reaction. After conjugation of PEG, an obvious peak is observed at 2942 cm^{-1} due to the stretching vibration of C–H in –CH_2– of PEG.

Figure 1a–j show TEM images and size distributions of MSN@MON, HMON, CON3-HMON, CON3-LAP-HMON@GF7, and CON3-LAP-HMON@GF7-ABS-PEG. The as-synthesized MSN@MON, HMON, and CON3-HMON exhibit similar spherical morphologies and decent monodispersity (Figure 1a–c f–h), with an average diameter of 43.8 ± 5.2, 47.2 ± 6.5, and 49.3 ± 4.0 nm, respectively. The hollow core is white for HMON, but black for CON3-HMON, which demonstrates that CON is successfully loaded inside the hollow core of CON3-HMON. CON3-LAP-HMON@GF7 and CON3-LAP-HMON@GF7-ABS-PEG still maintain the uniform spherical morphologies, but their hollow structures are completely not visible (Figure 1d,e), and their corresponding sizes respectively increase to 61.4 ± 8.4 and 68.0 ± 6.3 nm (Figure 1i,j), which suggest that the deposition of the GF layer and further modification of ABS and PEG are successful and the functionalization procedures do not affect the whole nanoparticle morphology and dispersity.

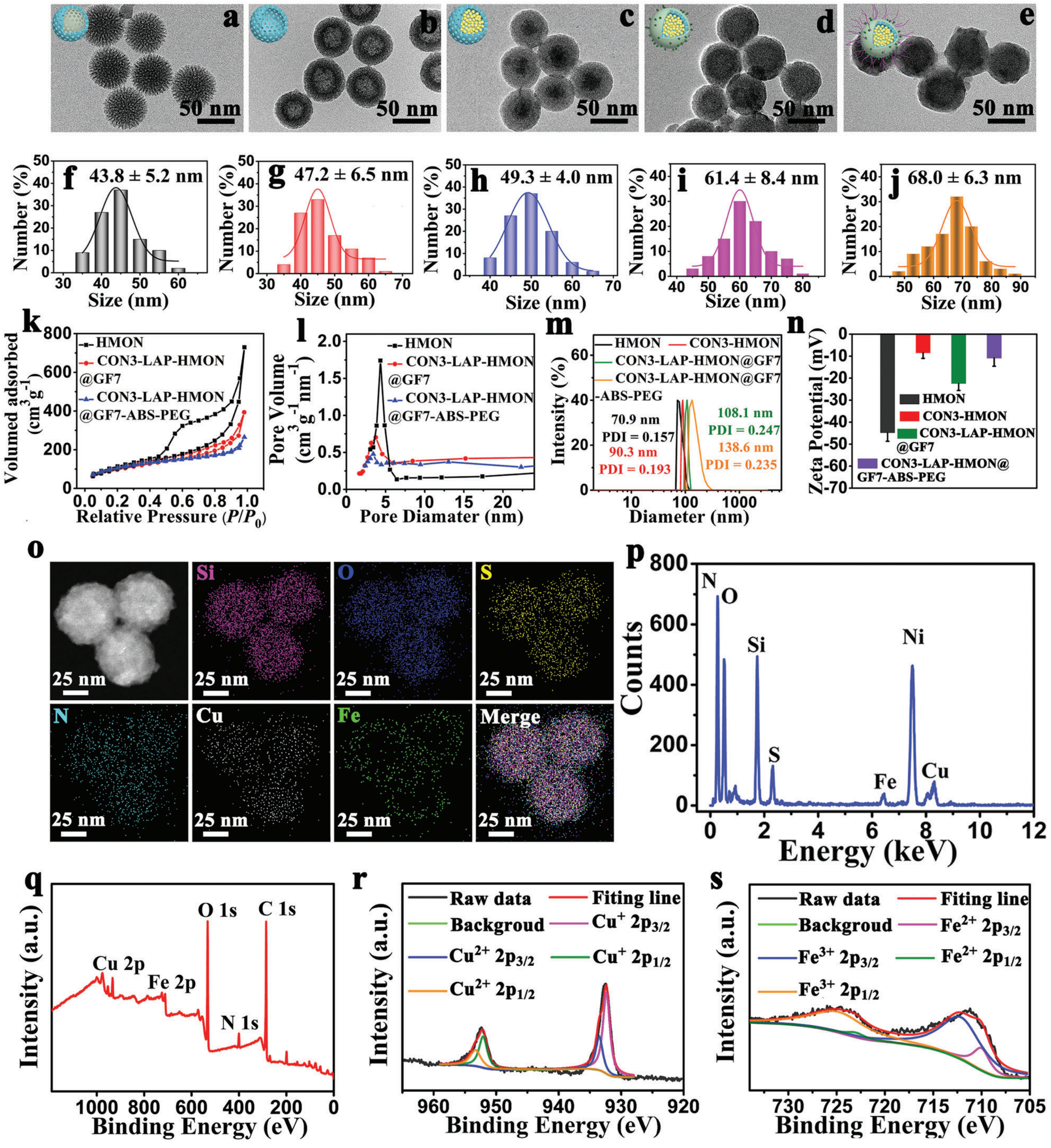

Figure 1. a–e) TEM images or f–j) size distributions of a,f) MSN@MON, b,g) HMON, c,h) CON3-HMON, d,i) CON3-LAP-HMON@GF7, or e,j) CON3-LAP-HMON@GF7-ABS-PEG. k) N_2 adsorption-desorption isotherms and l) pore size distributions of HMON, CON3-LAP-HMON@GF7, or CON3-LAP-HMON@GF7-ABS-PEG. m) Size distributions and n) Zeta potentials of various nanoparticles measured by DLS. o) STEM mappings, p) EDX spectrum, q) full range XPS spectra, and r) its corresponding high-resolution Cu 2p or s) Fe 2p XPS spectra for CON3-LAP-HMON@GF7-ABS-PEG.

The large surface area (565.0 $m^2\ g^{-1}$) and well-defined mesoporous structure (pore size ≈ 4.4 nm) of the HMON were examined by the typical N_2 adsorption-desorption method as shown in Figure 1k,l. After the successful coating of GF coordination layer and conjugation of ABS and PEG on the outer shell of HMON, the specific surface area respectively decreases to 315.9 and 172.1 $m^2\ g^{-1}$ (Figure 1k), and the corresponding pore size decreases to 3.7 and 3.3 nm, respectively (Figure 1l). Dynamic light scattering (DLS) results show that the average hydrodynamic diameters (d_h) are augmented along with the synthetic steps, which increase from 70.9 nm of HMON to 90.3 nm of CON3-HMON nm, 108.1 nm of

CON3-LAP-HMON@GF7, and 138.6 nm of CON3-LAP-HMON@GF7-ABS-PEG (Figure 1m). The Zeta potential of HMON, CON3-HMON, CON3-LAP-HMON@GF7, and CON3-LAP-HMON@GF7-ABS-PEG is −44.8, −8.5, −22.4, and −10.9 mv (Figure 1n), respectively. The corresponding changes of Zeta potentials for each functionalization step also demonstrate the successful preparation of nanocomplex. The CON3-LAP-HMON@GF7-ABS-PEG suspension with negative potentials contributes to strong electrostatic repulsion among the nanoparticles, displaying favorable colloidal stability in PBS buffer, DMEM medium, and DMEM medium plus fetal bovine serum (10%) even after 3 days of incubation at 37 °C (Figure S5, Supporting Information).

Scanning transmission electron microscopy (STEM)-associated energy-dispersive X-ray (EDX) elemental mapping analyses reveal that Cu mainly locates in the center, while Fe is confined to nano-shells of CON3-LAP-HMON@GF7-ABS-PEG nanopcomplex (Figure 1o). Other elements of Si, O, S, and N are homogeneously distributed throughout the nanocomplex (Figure 1o). The above-mentioned elements are all found in the EDX spectrum (Figure 1p). These results validate the successful synthesis of CON3-LAP-HMON@GF7-ABS-PEG with a core/shell structure.

X-ray photoelectron spectroscopy (XPS) reveals the representative peaks of C 1s, N 1s, O 1s, Fe 2p, and Cu 2p for CON3-LAP-HMON@GF7-ABS-PEG (Figure 1q–s, Figure S6a–c, Supporting Information). The high-resolution XPS spectrum of Cu 2p (Figure 1r) indicates two main peaks at 932.3 (Cu $2p_{3/2}$) and 952.1 eV (Cu $2p_{1/2}$) from Cu^+. The signals of Fe 2p (Figure 1s) are observed in 711.9 (Fe $2p_{3/2}$) and 725.0 eV (Fe $2p_{1/2}$) from Fe^{3+}. These results verify that the Cu and Fe of CON3-LAP-HMON@GF7-ABS-PEG exists primarily in the form of Cu^+ or Fe^{3+}, and the calculated percentages of Cu^+ or Fe^{3+} is 72.9% or 84.0% of total Cu or Fe amount, respectively.

2.2. pH/Glutathione Dual-Responsive Fenton-Catalytic Activity

The biodegradation behavior of CON3-LAP-HMON@GF7-ABS-PEG in mimic TME was directly evaluated by DLS and TEM measurements. Here, the final incubation condition (pH 6.5+10 mᴍ GSH) with better simulation of TME is selected for evaluating the degradation performance of nanoplatform in vitro, due to the pH value of the inherent TME is about 6.5.[11] Apparent attenuation of d_h from 138.9 ± 5.9 nm to 53.5 ± 8.2 is found for the nanocomplex after incubation with acidic buffer at pH 6.5 containing GSH (10 mᴍ) for 72 h (Figure S7a–d, Supporting Information). Moreover, TEM images (**Figure 2**a) show that CON3-LAP-HMON@GF7-ABS-PEG maintain intact structures after incubation in neutral conditions (pH = 7.4), reappears the visible hollow cores in acid conditions (pH = 6.5) because acid enables the release of the coating layer of GF-ABS-PEG and CON in cores, while the framework of CON3-LAP-HMON@GF7-ABS-PEG almost completely collapses in acidic buffer at pH 6.5 containing GSH (10 mᴍ). This specific pH/GSH dually responsive degradation of CON3-LAP-HMON@GF7-ABS-PEG would result in the on-demand release of therapeutic agents in TME (Figure 2b). As expected, the acidic conditions noticeably trigger the CON3-LAP-HMON@GF7-ABS-PEG biodegradation to release Fe, LAP, and Cu, and the reductive GSH further promotes their release (Figure 2c–e). Nearly 80% of the loaded Fe, LAP, and Cu are released within 24 h under acidic PBS (pH 6.5) with 10 mᴍ of GSH, whereas their released amount in PBS at pH 7.4 without GSH does not exceed 10%.

The Fenton-catalytic mechanism of CON3-LAP-HMON@GF7-ABS-PEG was assessed by the 3,3',5,5'-tetramethylbenzidine (TMB) assay (Figure 2f), which could be oxidized to oxTMB with blue or green color by the generated •OH. Because the efficiency of Fenton reaction to produce •OH is significantly dependent on pH conditions and our nanomedicine formula is designed to amplification acidity of TME, the final incubation condition (pH 6.0+10 mᴍ GSH) is exploited to study the Fenton catalytic activity of the CON3-LAP-HMON@GF7-ABS-PEG in vitro.

By comparing the Fenton-based reaction activity between CON3-HMON, HMON@GF7, and CON3-HMON@GF7 under same metal ion concentration, the efficiency of Fe/Cu-mediated catalytic cycle is further clarified (Figure S8, Supporting Information). As expected, the CON3-HMON@GF7 group shows significantly stronger absorbance of oxidized TMB at 652 nm (i.e., higher •OH generation capacity) than CON3-HMON or HMON@GF7 group. Because CON3-HMON@GF7 can release Fe^{3+} and Cu^+ simultaneously in response to acidic TME, resulting in the formation of Fe/Cu catalytic loop that substantially accelerates the interconversion between the metal ions with different oxidation states to derive the powerful Fenton catalytic performance. The findings demonstrate that the observed efficiency augment in the Fenton reaction mostly results from the Cu^+-mediated reduction of Fe^{3+} ions.

As shown in Figure 2g, the obvious TMB adsorption peak at 652 nm is detected in an acidic buffer containing H_2O_2 rather than a neutral solution. Especially, the group with GSH reveals the strongest performance of •OH generation owing to the GSH-responsive degradation, which results in fast release of metal ions involved in the Fenton reaction and corresponding high catalytic capacity. The time or H_2O_2-dependent capability of •OH generation is shown in Figure S9a,b, Supporting Information. The absorption peak at 650 nm increases with the extension of the reaction time or H_2O_2 concentration due to higher concentration of metal ions release and H_2O_2 are favorable for the production of •OH. Electron spin resonance (ESR) measurements further demonstrate the acid and GSH-triggered release of metal ions from CON3-LAP-HMON@GF7-ABS-PEG, which accelerates the rate of Fenton reaction with H_2O_2 and then produces the strongest characteristic peak of •OH in the ESR spectra (Figure 2h).

The GSH depletion ability of CON3-LAP-HMON@GF7-ABS-PEG was then measured by using 5, 5'-dithio-bis-2-(nitrobenzoic acid) as an indicator.[12] Since the released Fe^{3+} or Cu^{2+} can be reduced by GSH to Fe^{2+} or Cu^+, CON3-LAP-HMON@GF7-ABS-PEG has remarkable GSH depletion ability due to the faster release rate of metal ions under acidic conditions (Figure 2i). From Figure 2j, the absorption peak at 412 nm declines gradually with the extension of incubation time, indicating the extra depletion of GSH by CON3-LAP-HMON@GF7-ABS-PEG. That's because the HMON enriches in S–S bonds, which can also effectively undergo the redox reaction with GSH. Meanwhile, the concentration-dependent GSH consumption ability

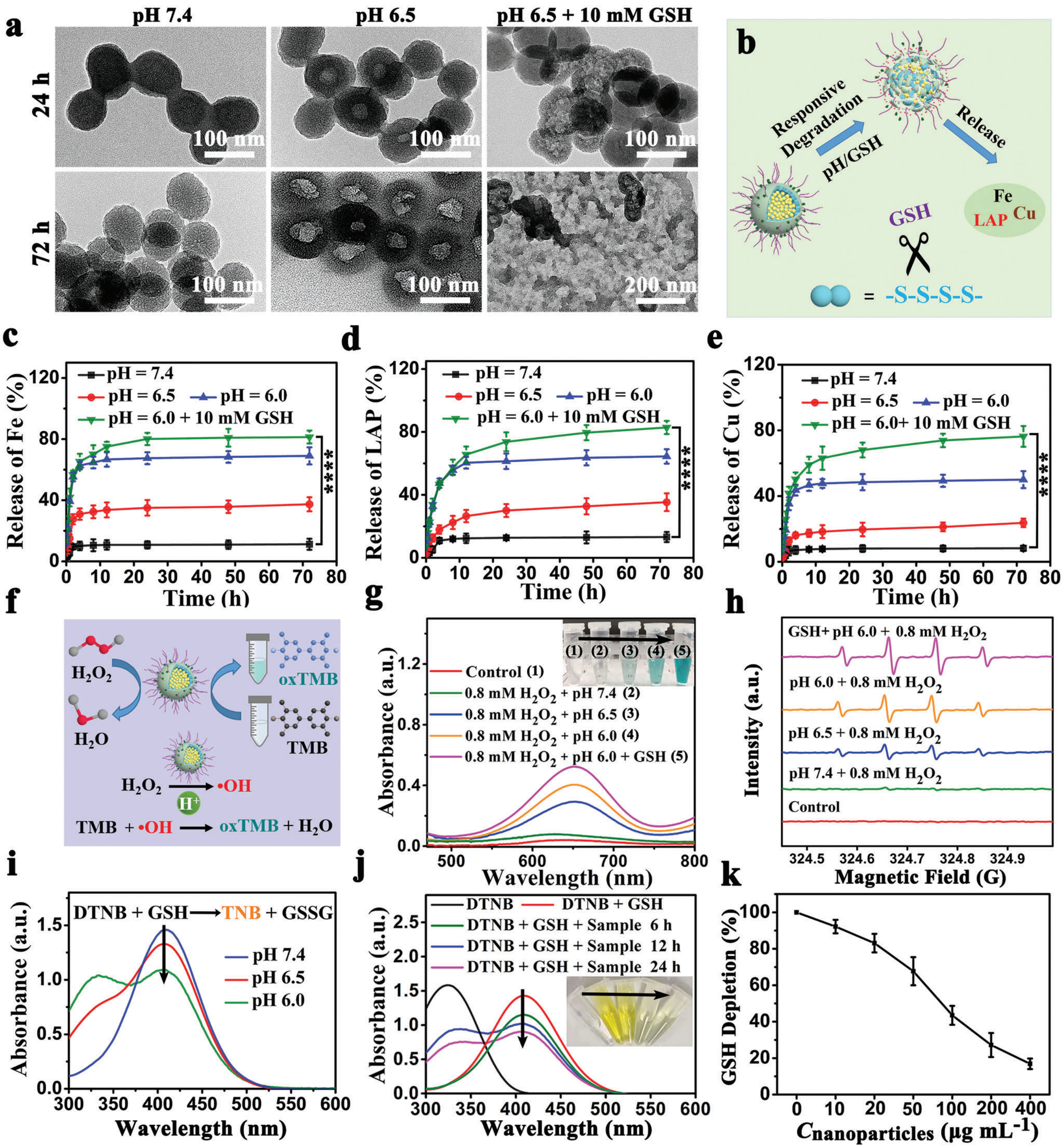

Figure 2. a) TEM images of biodegradable CON3-LAP-HMON@GF7-ABS-PEG after incubation at different conditions for 24 or 72 h. b) Schematic illustration of pH/GSH dually responsive degradation and release of theranostic components. Release curves of c) Fe, d) LAP, or e) Cu under neutral or acidic PBS with or without GSH. f) Schematic diagram for the Fenton-catalytic mechanism of CON3-LAP-HMON@GF7-ABS-PEG. g) UV–vis spectra and photographs (inset) of TMB aqueous solution treated with CON3-LAP-HMON@GF7-ABS-PEG under various conditions. h) ESR spectra under various conditions using 5,5-dimethyl-1-pyrroline-N-oxide (DMPO) as •OH trapping agent. i) pH dependence, j) time dependence, or k) concentration dependence of GSH consumption capacities for CON3-LAP-HMON@GF7-ABS-PEG nanoparticles using DTNB as an indicator. Data are presented as means ± SD ($n = 3$). ****$p < 0.0001$ determined by one-way ANOVA.

of CON3-LAP-HMON@GF7-ABS-PEG quantified from the constructed standard curve (Figure S10a,b, Supporting Information), is shown in Figure 2k, showing the favorable GSH depletion ability of CON3-LAP-HMON@GF7-ABS-PEG which would be conducive to the accumulation of ROS for cancer treatment through cascade catalysis.

2.3. Enhanced Cellular Uptake and Mechanism of Tumor Microenvironment Remodeling

CAIX, a transmembrane protein known to be regulated by hypoxia inducible factor, is regarded as an important active target because it is overexpressed in hypoxic solid tumors rather than in normal tissues and cells.[13] Importantly, CAIX with function of pH regulatory enzyme was reported to be able to reversibly catalyze the hydration of CO_2 to HCO_3^- and thus sustain the equilibrium of extracellular and intracellular pH values. The dysfunction of the CAIX enzyme by utilizing inhibitors is capable of increasing intracellular H^+ and establishing the acidic TME.[14] Therefore, the combination of nanocatalyzers with CAIX inhibitors is reasonably expected to be a promising strategy to significantly enhance the catalytic activity and efficacy of ferroptosis therapy.

To verify the specific recognization capability and internalization efficiency of nanocomplexes, the CAIX-positive 4T1 cells[15] were used. The CON3-HMON@GF7-PEG and CON3-HMON@GF7-ABS-PEG were labeled with rhodamine6G (R6G) to realize visual observation of their fluorescence. From laser scanning confocal microscopy (LSCM) images (**Figure 3**a, Figure S11, Supporting Information), it is found that the 4T1 cells treated with R6G-labeled CON3-HMON@GF7-ABS-PEG display stronger red fluorescence signals than that treated with the R6G-labeled CON3-HMON@GF7-PEG under either normoxia or hypoxia. Especially, the cells incubated with R6G-labeled CON3-HMON@GF7-ABS-PEG after hypoxia-induction possesses the highest uptake level of nanoparticles by 4T1 cells. Further flow cytometry results (Figure 3b,c) also show that the fluorescence intensities of the R6G-labeled CON3-HMON@GF7-ABS-PEG (hypoxia) group are much stronger than the group of R6G-labeled CON3-HMON@GF7-PEG (normoxia) ($^{***}P < 0.001$) or CON3-HMON@GF7-ABS-PEG (normoxia) ($^{*}p < 0.05$). This enhanced cellular uptake of R6G-labeled CON3-HMON@GF7-ABS-PEG can be attributed to the CAIX-targeting mediated endocytosis based on the linkage of ABS on the surface of nanocomplex, which has the CAIX binding ability.[16] Since the level of CAIX expression is further increased by hypoxia,[17] the promotion of binding performance results in higher internalization efficiency under a hypoxic atmosphere.

To validate the capability of CON3-LAP-HMON@GF7-ABS-PEG for potentiating acidic TME, the variations of tumor intracellular pH value were measured via a pH-sensitive probe of 2',7'-bis-(2-carboxyethyl)-5-(and-6)-carboxyfluorescein, acetoxymethyl ester,[18] whose fluorescence decreases with acid increase (Figure S12, Supporting Information). CSLM observations reveal that the 4T1 cells treated by PBS, LAP, CON3-HMON@GF7-PEG, or CON3-LAP-HMON@GF7-PEG have no obvious difference in intracellular pH under normoxia or hypoxia (Figure S13, Supporting Information, the first row of Figure 3h), while a slight decrease of green fluorescence is found in CON3-LAP-HMON@GF7-ABS-PEG treated group (normoxia), and an obvious decrease of green fluorescence is observed in CON3-LAP-HMON@GF7-ABS-PEG treated group (hypoxia). That's because the inhibition of over-expressed CAIX by the loaded ABS can cause the accumulation of intracellular acidic ions.[17] Consistently, the flow cytometry analysis (Figure 3d) and its corresponding quantitative results (Figure 3e) also show that only CON3-LAP-HMON@GF7-ABS-PEG treated group under hypoxia can weaken the intensity of green fluorescence, that is, decrease the intracellular pH value. These results indicate that the ABS-mediated CAIX suppression can specifically down-regulate the tumor intracellular pH to re-establish tumor acidic conditions, and thereby overcome the intrinsically insufficient acidity of the TME to enhance the Fenton-reaction efficiency.

The capability of our CON3-LAP-HMON@GF7-ABS-PEG for intracellular GSH depletion and GSH peroxidase 4 (GPX4) inactivation was quantified by using the Assay Kit technique. The incubation of CON3-LAP-HMON@GF7-ABS-PEG causes the conspicuous down-regulation of GSH level ($^{***}p < 0.001$, $^{*}p < 0.05$) and GPX4 activity ($^{***}p < 0.001$, $^{*}p < 0.05$) compared with that incubated with PBS or CON3-LAP-HMON@GF7-PEG group (Figure 3f,g), which is ascribed to the CAIX-mediated active targeting effect, and the enhanced intracellular acidic condition by ABS. The regulated TME (i.e., more acidic condition) is capable to promote the release of Fe^{3+} and Cu^+ ions efficiently, accelerate the Fenton and Fenton-like reactions due to the catalytic loop of Fe–Cu, and then lead to the significant GSH consumption and subsequent GPX4 inactivation.

Similar results can be found from the LSCM images of 4T1 cells after various treatments and staining with Thiol Tracker Violet, showing intracellular GSH with green fluorescence (Figure S14, Supporting Information). It is noted that GSH levels in 4T1 cells treated with LAP or LAP-loaded nanoparticles were markedly depleted because LAP not only supplies H_2O_2 by a catalytic cycle of the NADPH and NQO1 enzyme (overexpressed in tumor cells), but also down-regulates GSH levels in tumor cells due to the coenzyme (NADPH) consumption of reductive GSH via the LAP-triggered redox cycle.[19] Figure S15, Supporting Information, shows the apparent increase of $NADP^+$/NADPH ratio after treatment of LAP or LAP-loaded nanocomplexes compared with the PBS group ($^{*}p < 0.05$, $^{**}p < 0.01$). The H_2O_2 production induced by LAP is in a concentration-dependent manner (Figure S16, Supporting Information), validating the simultaneous inhibition of NAPDH and promotion of H_2O_2 generation based on catalysis of LAP futile cycle through NQO1-mediation.

Inspiring the above considerable GSH depletion effect, the intracellular ROS level after different treatments were monitored by the DCFH-DA staining assay. From the LSCM images as shown in Figure 3h (the second row) and Figure S17, Supporting Information, it is found that CON3-LAP-HMON@GF7-PEG treated group (IV) reveals increased ROS production compared with LAP (II) and CON3-HMON@GF7-PEG group (III), which indicates that the successful LAP delivery enhances the H_2O_2 generation based on the NQO1-mediated redox cycle and then further accelerates the Fenton and Fenton-like reactions. The CON3-LAP-HMON@GF7-ABS-PEG treated group (V) results in more enhanced ROS production compared with the CON3-LAP-HMON@GF7-PEG group (IV), which demonstrates that the ABS

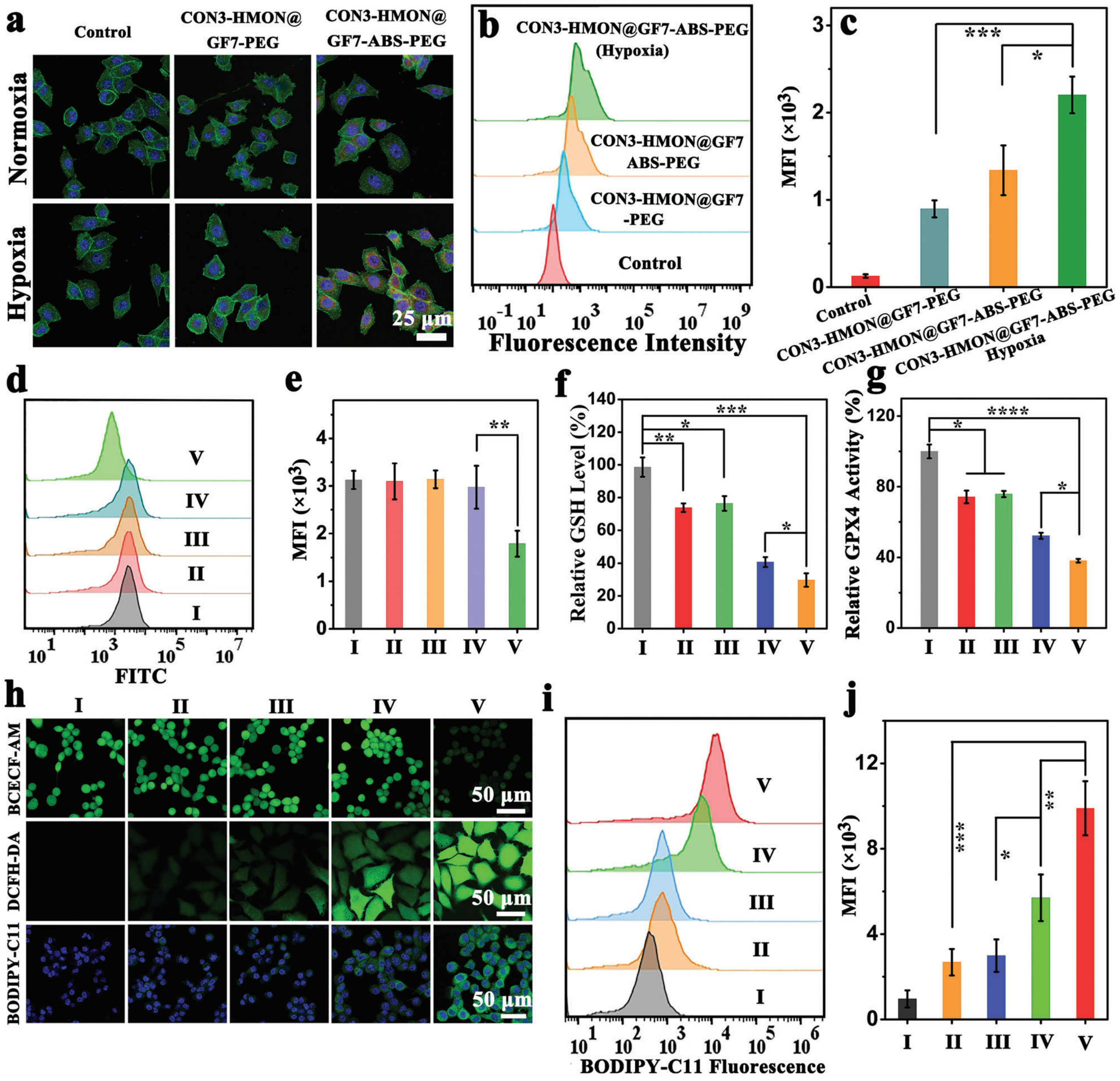

Figure 3. a) LSCM images of 4T1 cells incubated with the R6G-labelled CON3-HMON@GF7-PEG or CON3-HMON@GF7-ABS-PEG in both normoxia and hypoxia conditions. b) Fluorescence distributions and c) corresponding quantitative analysis of 4T1 cells incubated with various formulations measured by flow cytometry. d) Fluorescence distributions and e) corresponding quantitative analysis of 4T1 cells treated with I) PBS, II) LAP, III) CON3-HMON@GF7-PEG, IV) CON3-LAP-HMON@GF7-PEG, or V) CON3-LAP-HMON@GF7-ABS-PEG in the hypoxic atmosphere, and stained with BCECF-AM. f) GSH levels or g) GPX4 activity of 4T1 cells under hypoxia treated with the formulations of I–V. h) LSCM images indicating intracellular H^+, ROS, or LPO in 4T1 cells treated with the formulations of I–V under hypoxia, and stained with BCECF-AM, DCFH-DA, or BODIPY-C11. i) Fluorescence distributions and j) corresponding quantitative analysis of LPO levels (measured by flow cytometry) in 4T1 cells treated with the formulations of I–V, and stained with BODIPY-C11. Data are presented as means ± SD ($n = 3$). $^*p < 0.05$, $^{**}p < 0.01$, $^{***}p < 0.001$, and $^{****}p < 0.0001$ determined by one-way ANOVA.

functions of CAIX-mediated active targeting and more acidic TME establishing can also accelerate the Fenton and Fenton-like reactions. Furthermore, the green fluorescent ROS stained with DCFH-DA in the CON3-LAP-HMON@GF7-ABS-PEG treated group (V) under hypoxia conditions is much stronger than that under normoxia conditions, indicating that the CAIX expression can be further increased by hypoxia.

Because large amounts of ROS can result in the accumulation of LPO within 4T1 cancer cells, the LPO level was subsequently evaluated via the BODIPY-C11 staining assay. Significant promotion of green LPO fluorescence signal begins to appear in the CON3-LAP-HMON@L@GF7-PEG group, and the highest LPO level is observed in the CON3-LAP-HMON@GF7-ABS-PEG group (Figure S18, Supporting Information, and the third row of

Figure 3h), which is similar with the ROS signals as shown in the second row of Figure 3h and Figure S17, Supporting Information. The fluorescence distributions (Figure 3i) and corresponding quantitative analysis (Figure 3j) of the LPO levels (measured by flow cytometry) in 4T1 cells show similar outcomes.

Figure S19, Supporting Information, shows LSCM images of 4T1 cells after treatment with CON3-LAP-HMON@GF7-PEG, or CON3-LAP-HMON@GF7-ABS-PEG for 4.0 h. It is found that lots of green fluorescence (RhoNox-1 for Fe^{2+}) does not overlap with the red fluorescence (Lysotracker Red for lysosomes), which demonstrates the lysosomal escape of our nanoparticles that is the prerequisite for the following Fenton reaction cycloacceleration and ferroptosis therapy.

2.4. In Vitro High-Performance Ferroptosis

Figure 4a shows the schematic mechanism illustration of CON3-LAP-HMON@GF7-ABS-PEG for high-performance ferroptosis therapy of tumors based on the strategy of Fenton reaction cycloacceleration initiated by regulating TME, including acidification of intracellular pH value, self-supply of H_2O_2, depletion of intracellular GSH, robust ROS generation, and accumulation of LPO to synergistically enhance intracellular oxidative stress. The in vitro anticancer efficacy was further investigated for substantiating the augmented ferroptosis via the strategy of Fenton reaction cycloacceleration.

Figure 4b exhibits the lower toxicity of CON3-LAP-HMON@GF7-ABS-PEG on CAIX-negative HeLa cells than CAIX-positive 4T1 cells ($*p < 0.05$) due to the limited Fenton catalytic efficiency in the cells with low expression of CAIX (i.e., insufficient acidic conditions). Furthermore, compared with CAIX-positive 4T1 cells (36.8% ± 1.4%) under the same treatment conditions, nanomedicines maintain a relatively high cell viability on HUVECs (67.1% ± 6.1%, $***p < 0.001$). That's because the normal HUVECs with simultaneously low expression of CAIX and NQO1 is difficult to realize the robust generation of H^+, H_2O_2, and •OH (Scheme 1). Therefore, the high-performance ferroptosis therapy is only applicable to the CAIX-overexpressing cancer cells, revealing the high tumor specificity of ferroptosis therapy strategy based on our CON3-LAP-HMON@GF7-ABS-PEG. Concentration-dependent cytotoxicity of CON3-LAP-HMON@GF7-ABS-PEG against 4T1 cancer cells was then observed in both normoxic and hypoxic atmospheres (Figure 4c). As the hypoxia induces further elevation of CAIX in 4T1 cancer cells, CON3-LAP-HMON@GF7-ABS-PEG presents a higher killing performance in hypoxia than in normoxia. By comparing the cytotoxicity of various treatment groups (Figure 4d), it is found that the anticancer effect of CON3-LAP-HMON@GF7-ABS-PEG is significantly stronger than that of PBS, LAP, CON3-HMON@GF7-P, or CON3-LAP-HMON@GF7-PEG after 24 h of treatment ($**p < 0.01$ or $***p < 0.001$), whereas the cytotoxicity of CON3-LAP-HMON@GF7-ABS-PEG alleviates with the addition of ferrostatin-1 (Fer-1, an inhibitor of ferroptosis) ($**p < 0.01$). Figure S20, Supporting Information, shows negligible cytotoxicity of free ABS against 4T1 cancer cells under normoxia or hypoxia. These results demonstrate that the higher cytotoxicity of CON3-LAP-HMON@GF7-ABS-PEG than CON3-LAP-HMON@GF7-PEG can be ascribed to the augmented ferroptosis based on the CAIX-mediated active targeting and intracellular acidification by ABS.

Previous reports have demonstrated that inordinate ROS can result in mitochondrial impairments.[20] The various treatment-induced changes of mitochondrial membrane potential were evaluated by JC-1 staining assay. As shown in Figure 4e, the evident decrease of JC-1 aggregates (red spots) and the significant augment of JC-1 monomers (green spots) are found in the CON3-LAP-HMON@GF7-PEG group (IV) compared with PBS (I), LAP (II), and CON3-HMON@GF7-PEG (III) groups, indicating the decline of mitochondrial membrane potential and the mitochondrial damage. More severe mitochondrial dysfunction can be observed from the 4T1 cancer cells treated with CON3-LAP-HMON@GF7-ABS-PEG (V) under hypoxia, demonstrating the robust ROS generation.

Meanwhile, the ferroptosis efficacy of CON3-LAP-HMON@GF7-ABS-PEG in vitro was assessed by propidium iodide (PI, for dead cells) and calcein AM (for live cells) co-staining assay, and Annexin V/propidium iodide (PI) apoptosis assay kit, respectively. From Figure 4f, it can be seen that large amounts of dead cells (red dots) only occur in the CON3-LAP-HMON@GF7-PEG (IV) and CON3-LAP-HMON@GF7-ABS-PEG group (V), rare live cells are observed from CON3-LAP-HMON@GF7-ABS-PEG group (V), whereas the LAP (II) and CON3-HMON@GF7-PEG (III) still maintain a high level of live cells (green dots) owing to the limited ROS generation. Further analysis of 4T1 cells apoptosis (Figure 4g,h) displays a similar trend to the Live-Dead staining results. Notably, the CON3-LAP-HMON@GF7-ABS-PEG (V) exhibits a greater apoptosis rate compared to other treatment groups ($**p < 0.01$, $***p < 0.001$). The results manifest the high-performance ferroptosis induced by Fenton reaction cycloacceleration initiated by the catalytic loop of Fe–Cu, the ABS functions of CAIX-mediated active targeting and more acidic condition establishing, and the in situ H_2O_2 generation from the LAP-triggered and NQO1-mediated redox cycle.

2.5. Enhanced T_1-Weighted Magnetic Resonance Imaging and In Vivo Biodistribution

T_1-weighted MR images, and the corresponding $1/T_1$ or $1/T_2$ linear fitting results of CON3-LAP-HMON@GF7-ABS-PEG determined by a MRI scanner system (3.0 T) are shown in **Figure 5**a,b, and Figure S21, Supporting Information. The longitudinal relaxivity (r_1) and transverse relaxivity (r_2) are respectively 1.8 and 12.1 $\text{mM}^{-1}\ \text{s}^{-1}$ calculated from the slopes of the linear lines of T_1/T_2 relaxation rates versus Fe concentrations (C_{Fe}), which exhibits a relatively weak MRI signal due to the high r_2/r_1 ratio (6.7). Based on the TME-activatable degradation capability, the longitudinal/transverse relaxation time (T_1/T_2) of CON3-LAP-HMON@GF7-ABS-PEG with varied C_{Fe} incubated with acidic buffer at pH 6.5 containing 10 mM GSH (i.e., simulated TME) for 24 or 48 h were also assessed at 3.0 T. A conspicuous simulated TME-triggered brightness enhancement of T_1-weighted MR images with the increase of incubation time is found in Figure 5a. The r_1 value of CON3-LAP-HMON@GF7-ABS-PEG augments from 1.8 to 4.2 $\text{mM}^{-1}\ \text{s}^{-1}$ (Figure 5b), and corresponding

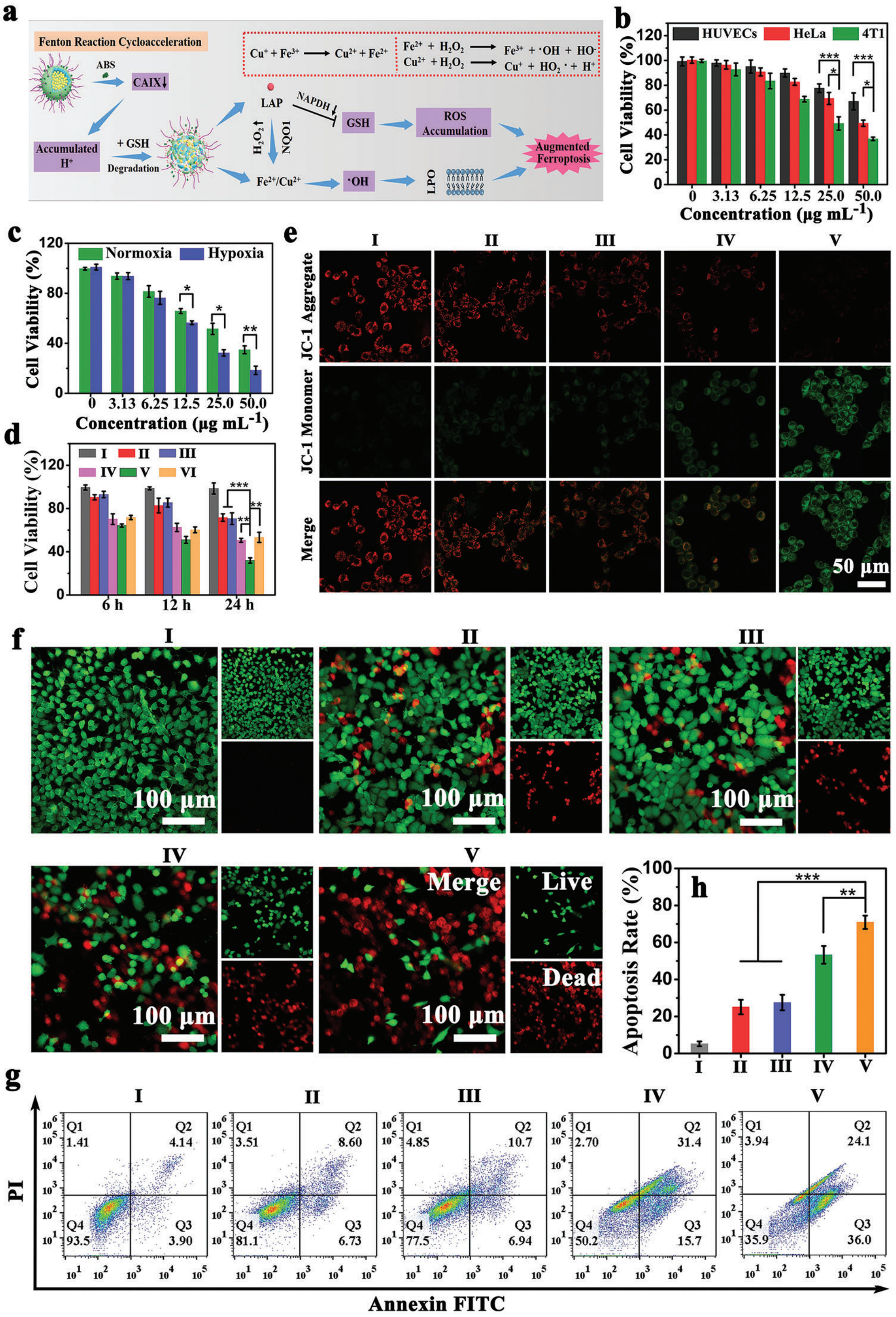

Figure 4. a) Schematic mechanism illustration of CON3-LAP-HMON@GF7-ABS-PEG for high-performance ferroptosis therapy of tumors based on the strategy of Fenton reaction cycloacceleration initiated by regulating TME. b) Cytotoxicity evaluation of CON3-LAP-HMON@GF7-ABS-PEG on HUVECs, HeLa (CAIX-negative expression), or 4T1 (CAIX-positive expression) cells under normoxia ($n = 5$). c) Cell viabilities of CON3-LAP-HMON@GF7-ABS-PEG in 4T1 cells in both normoxic and hypoxic conditions ($n = 5$). d) Time-dependent cytotoxicity of 4T1 cells after incubation with I) PBS, II) LAP, III) CON3-HMON@GF7-PEG, IV) CON3-LAP-HMON@GF7-PEG, V) CON3-LAP-HMON@GF7-ABS-PEG, or VI) CON3-LAP-HMON@GF7-ABS-PEG including Fer-1 (50 nM) under hypoxia ($n = 5$). e) Confocal images of 4T1 cells after treatment with the formulations of I–V under hypoxia stained with JC-1 dye or f) co-stained calcein-acetoxymethyl (AM) for live cells and propidium iodide (PI) dead cells. g,h) Measurement of cell apoptosis by annexin V-FITC/PI double staining after 4T1 cells being treated with various formulations under hypoxia ($n = 3$). Data are presented as means ± SD. $^*p < 0.05$, $^{**}p < 0.01$, and $^{***}p < 0.001$ determined by one-way ANOVA.

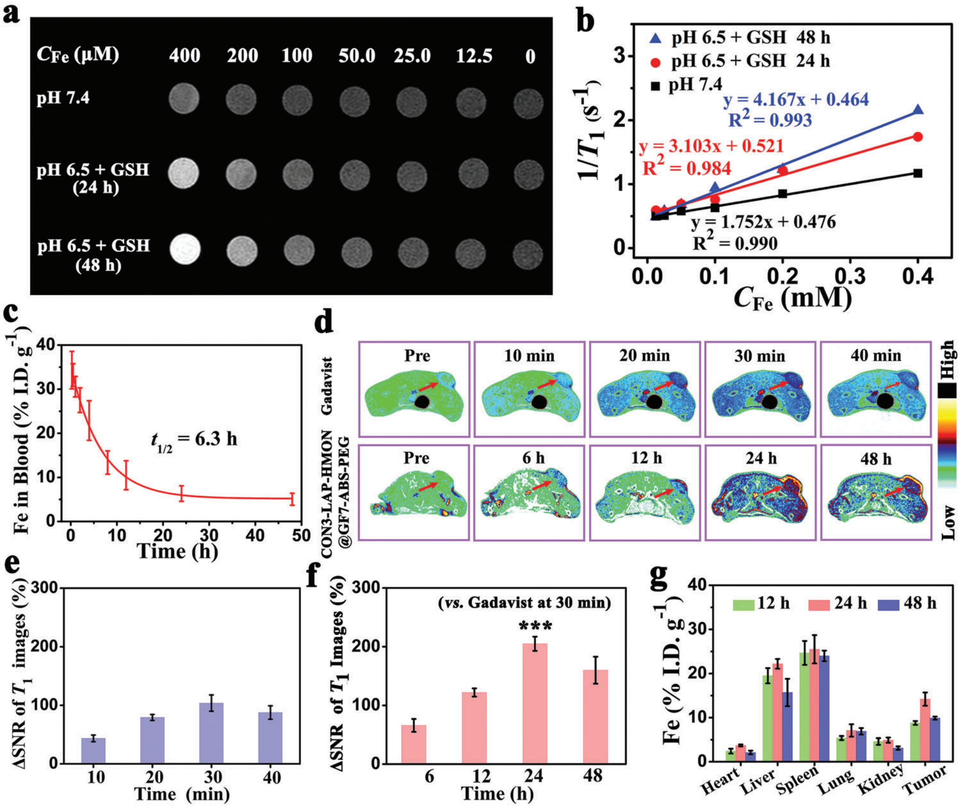

Figure 5. a) T_1-weighted MR images of CON3-LAP-HMON@GF7-ABS-PEG solutions with different C_{Fe}, incubated at pH 7.4 for 48 h, or at pH 6.5 with 10 mM GSH for 24 or 48 h. b) Corresponding T_1 relaxation rates (1/T_1) as a function of the C_{Fe}. c) Blood circulation curve of CON3-LAP-HMON@GF7-ABS-PEG in mice after i.v. injection. d) T_1-weighted MR images of 4T1 tumor-bearing mice pre- and post-injection of commercial Gadavist or CON3-LAP-HMON@GF7-ABS-PEG (Gd or Fe dosage is 5.0 mg kg^{-1}) at different time intervals. e) Quantitative analysis for the tumor MR images post-injection of Gadavist or f) CON3-LAP-HMON@GF7-ABS-PEG. g) Biodistribution of Fe in major organs and tumors of mice intravenously injected with CON3-LAP-HMON@GF7-ABS-PEG at predetermined time points. Data are presented as means ± SD (n = 3). ***$p < 0.001$ determined by one-way ANOVA.

r_2/r_1 ratio attenuates from 6.7 to 4.8 even the r_2 value also exhibits a certain increase from 12.1 to 19.9 mM^{-1} s^{-1} (Figure S21, Supporting Information). The TME-responsive MRI contrast enhancement can be ascribed to the improvement of interaction between water protons and GF networks released from CON3-LAP-HMON@GF7-ABS-PEG in response to the simulated TME, which provides the considerable possibility for MRI-guided tumor therapy.

Prior to in vivo MRI evaluation, the blood circulation half-life is determined to be 6.3 h after intravenous (i.v.) injection of CON3-LAP-HMON@GF7-ABS-PEG (Figure 5c). Figure 5d shows the T_1-weighted MRI performance of tumors at different time points post-injection of various contrast agents. Significant MRI signal enhancement in tumor sites is observed from CON3-LAP-HMON@GF7-ABS-PEG injected group, and the highest brightness can be seen at 24 h. The comparatively low signal of 4T1 tumor-bearing mice administrated with commercial Gadavist peaks at 30 min, which is accompanied by the rapid renal excretion of the small molecular Gd chelates.[21] Meanwhile, the corresponding quantitative results of signal-to-noise ratio (SNR) presents durable MRI signal with bright contrast intensity to tumor sites for CON3-LAP-HMON@GF7-ABS-PEG (Figure S22, Supporting Information), and the ΔSNR shows a higher contrast of CON3-LAP-HMON@GF7-ABS-PEG than Gadavist (***$p < 0.001$, Figure 5e,f), which demonstrates the efficient tumor-specific accumulation and TME-enabled enhancement of T_1 MRI for our CON3-LAP-HMON@GF7-ABS-PEG nanocomplex.

The evaluation of in vivo biodistribution shows the highest enrichment (14.2% ± 1.5% I.D. g^{-1}) of Fe in tumor tissues at 24 h post-injection of CON3-LAP-HMON@GF7-ABS-PEG (Figure 5g), which is consistent with the above-mentioned blood circulation half-life and MRI results. This appreciable tumor accumulation of CON3-LAP-HMON@GF7-ABS-PEG further validates the strengthened EPR effect and CAIX-mediated active targeting.

2.6. In Vivo Assessments on Therapeutic Efficacy and Biosafety

In vivo ferroptosis therapy efficacy after i.v. injection of (I) PBS, (II) LAP, (III) CON3-HMON@GF7-PEG, (IV) CON3-LAP-HMON@GF7-PEG, or (V) CON3-LAP-HMON@GF7-ABS-PEG was also examined by using 4T1 tumor-bearing mice (**Figure 6**a). From the tumor growth curves (Figure 6b) and the tumor inhibition rates at the 20th day (Figure 6c), rapid tumor growth for PBS treated group, partial suppression of tumor growth for LAP and CON3-HMON@GF7-PEG group, and noticeable antitumor effect for CON3-LAP-HMON@GF7-PEG

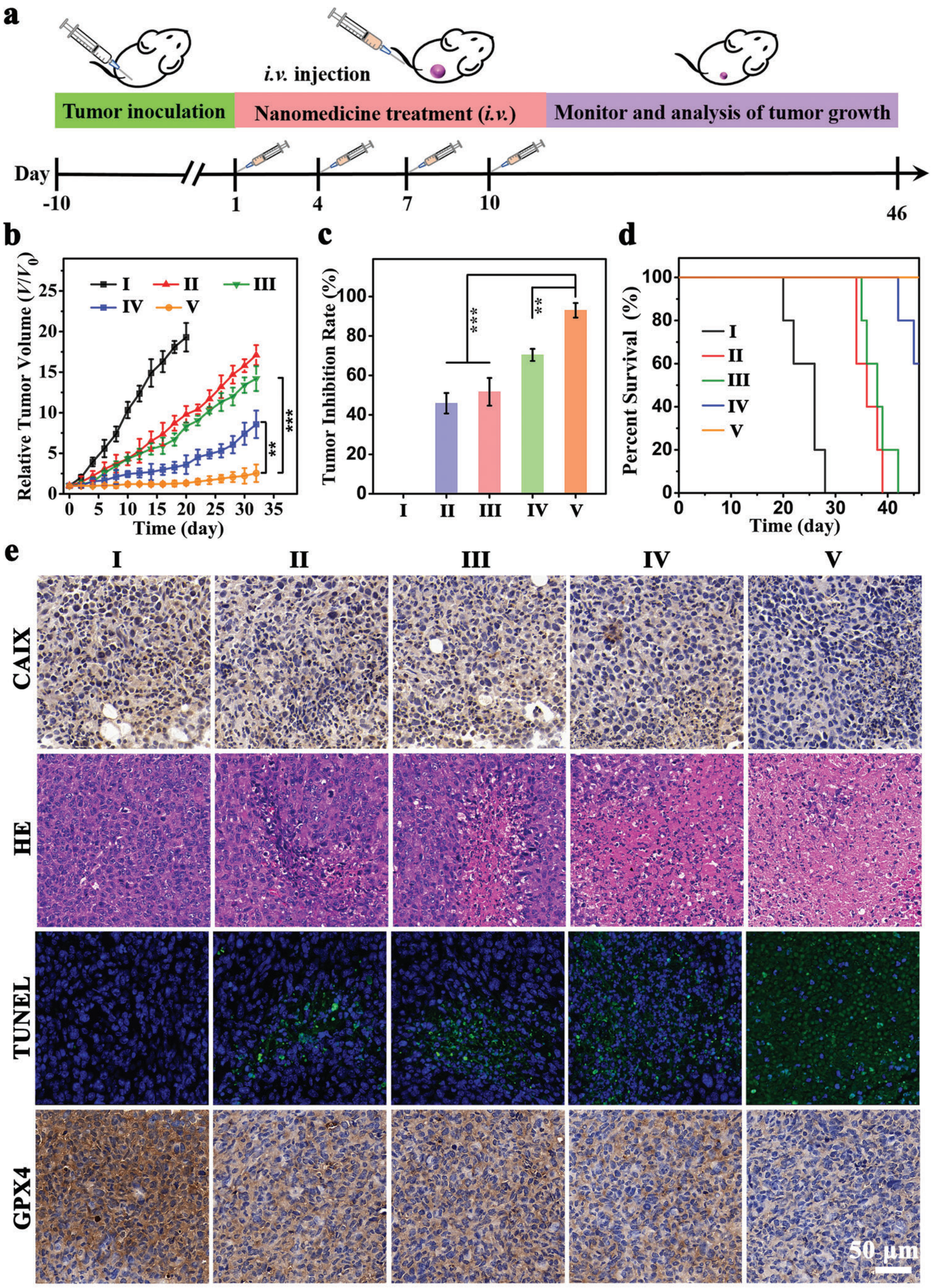

Figure 6. a) Schematic illustration of the treatment schedule in vivo. b) Relative tumor volumes, c) tumor inhibition rate at the 20th day, or d) survival curves of 4T1 tumor-bearing mice after being treated by I) PBS, II) LAP, III) CON3-HMON@GF7-PEG, IV) CON3-LAP-HMON@GF7-PEG, or V) CON3-LAP-HMON@GF7-ABS-PEG. e) CAIX, H&E, TUNEL, or GPX4 staining of representative tumors collected from the I–V groups. Data are presented as means ± SD ($n = 5$). $^{**}p < 0.01$, and $^{***}p < 0.001$ determined by one-way ANOVA.

and CON3-LAP-HMON@GF7-ABS-PEG group are found. Especially, CON3-LAP-HMON@GF7-ABS-PEG administrated group achieves a tumor inhibition rate of over 90%. Besides, survival rates of 4T1 tumor-bearing mice treated by CON3-LAP-HMON@GF7-ABS-PEG remain at 100% within 46 days (Figure 6d), which is much superior to that of other administrated groups, suggesting the high-performance tumor ferroptosis therapy of CON3-LAP-HMON@GF7-ABS-PEG.

The collected tumor tissues from the sacrificed mice after various treatments were stained with hematoxylin and eosin (H&E), CAIX, GPX4, and terminal deoxynucleotidyl transferase dUTP nick end labeling (TUNEL) to further explore the mechanism of antitumor therapy. It can be clearly found that the obvious downregulation of CAIX expression only occurs in the CON3-LAP-HMON@GF7-ABS-PEG group (Figure 6e), which is ascribed to the specific delivery of ABS to tumor tissues resulting in the strong inhibition of CAIX. Both H&E and TUNEL staining results show severely necrotic or apoptotic tumor cells in the CON3-LAP-HMON@GF7-ABS-PEG group, while relatively low or few numbers of such cells are observed in other groups. Consistently, the CON3-LAP-HMON@GF7-ABS-PEG treated mice show the most apparent downregulation of GPX4 expression and the strongest green fluorescence distribution of ROS or LPO (Figure S23, Supporting Information), further revealing the enhanced ferroptosis effect via the strategy of Fenton reaction cycloacceleration.

Figure S24, Supporting Information, shows the much lower hemolysis percentages (less than 2.0%) of CON3-LAP-HMON@GF7-ABS-PEG with varied concentrations. There are slight weight changes gained in 4T1 tumor-bearing mice after various treatments within 32 days (Figure S25, Supporting Information). No conspicuous histopathological aberration in major organs (heart, liver, spleen, lung, and kidney) is found for various treatment groups (Figure S26, Supporting Information). In addition, the blood routine analysis (including RBC, WBC, PLT, HCT, LYM, and HGB, Figure S27, Supporting Information) or blood biochemical analysis (including ALT, AST, ALP, and CREA, Figure S28, Supporting Information) of healthy mice after i.v. injection of CON3-LAP-HMON@GF7-ABS-PEG shows an unnoticeable difference for all testing parameters compared with the PBS group (control). These results suggest the favorable biosafety of our CON3-LAP-HMON@GF7-ABS-PEG nanocomplexes used for MRI-guided high-performance ferroptosis therapy based on the strategy of Fenton reaction cycloacceleration initiated by remodeling the TME.

3. Conclusions

In summary, we propose a strategy of Fenton reaction cycloacceleration initiated by remodeling the TME for MRI-guided high-performance ferroptosis therapy of tumors. Typically, the hollow core of HMON is utilized as a nanoreactor for “in situ CON growth” via a hydrazine reduction method, and then the LAP as a donor of H_2O_2 and GF coordination network are sequentially integrated into the pore channel and outer shell of HMON, which is further conjugated with ABS and PEG by typical amidation reaction to produce CON3-LAP-HMON@GF7-ABS-PEG. This successful preparation has been verified by TEM, DLS, Zeta potential analysis, STEM-based elemental mapping, XPS, UV–vis spectra, FT-IR, and BET. The CON3-LAP-HMON@GF7-ABS-PEG exhibits enhanced accumulation at CAIX-positive tumors based on the CAIX-mediated active targeting, and increased acidification via the inhibition of CAIX by ABS (i.e., remodeling TME). This accumulated H^+ and abundant GSH in TME synergistically trigger biodegradation of CON3-LAP-HMON@GF7-ABS-PEG to release the loaded CON, LAP, Fe^{3+}, and GF. The released CON reacts with the increased H^+, generating Cu^+. The Fe^{3+} reacts with Cu^+, producing Fe^{2+} and Cu^{2+} to accelerate the Fenton and Fenton-like reactions based on the catalytic loop of Fe–Cu. The released LAP produces H_2O_2 in situ from the LAP-triggered and NQO1-mediated redox cycle to further accelerate the Fenton and Fenton-like reactions. The cycloacceleration of Fenton and Fenton-like reactions initiated by remodeling TME generates robust ROS and plenitudinous LPO accumulation for high-performance ferroptosis of tumor cells. In addition, the GF network detached from HMON has a relatively high r_1 (4.2 mм$^{-1}$ s^{-1}) and low r_2/r_1 ratio (4.8) in response to the TME, which is successfully utilized as a favorable T_1-weighted MRI contrast agent to monitor the progress of tumor ferroptosis therapy. Overall, the strategy of Fenton reaction cycloacceleration initiated by remodeling the TME via our CON3-LAP-HMON@GF7-ABS-PEG is promising for MRI-guided high-performance ferroptosis therapy of tumors.

4. Experimental Section

Synthesis of CON1-4-HMON: PVP (10–80 mg) was first added into 10 mL of HMON aqueous solution, which was stirred at room temperature for 45 min. 1.0 mL of copper precursor solutions (25–200 mм $CuCl_2 \cdot 2H_2O$) were then respectively charged into the above solution under magnetic stirring. The pH value of the mixtures was tuned to 9.0 using NaOH (1.0 м). The solutions was then preheated to 60 °C in an oil bath and stirred for 30 min under N_2 protection. After that, reducing hydrazine hydrate (5.0–40 µL) was added into the above systems and the reaction was continued for 120 min until the solutions turned yellow. The remaining sediments were purified by centrifugation (20 000 × *g*, 10 min) and washed with pure water for five cycles to obtain the in situ CON generated in the hollow core of HMON (CON1-4-HMON), which were redispersed in Milli-Q water for further use.

Synthesis of CON3-HMON@GF1-8: 50 µL of $FeCl_3$ solution (1.3–40 mg mL^{-1}) was respectively added into CON3-HMON dispersions (1.0 mL, 5.0 mg mL^{-1}). After continuous stirring for 15 min, 100 µL of GA aqueous solution (10 or 20 mg mL^{-1}) with pH value of 8.0 was added dropwise into the above suspensions, and the mixtures were kept under stirring for 2.0 h to finish the coordination reaction between Fe^{3+} and GA. CON3-HMON@GF1-8 was then obtained by centrifugation and washing with MilliQ water. The Fe or Cu loading content was determined by ICP-OES (Thermo Fisher Scientific, iCAP 6300Duo). The CON3-HMON@GF7 were fabricated with 1.0 mg mL^{-1} of $FeCl_3$ and 2.0 mg mL^{-1} of GA for the following experiments.

Synthesis of CON3-LAP-HMON@GF7: The CON3-HMON dispersion (4.0 mL, 2.5 mg mL^{-1}) was first mixed with 1.0 mL of ethanolic LAP solution (2.0 mg mL^{-1}), and the mixture was kept under stirring overnight at room temperature away from the light. After that, the obtained solution was centrifuged (20 000 × *g*, 10 min) and washed to obtain CON3-LAP-HMON. The CON3-LAP-HMON was used to synthesize CON3-LAP-HMON@GF7 according to the above-mentioned procedures. The final product was obtained after centrifugation (20 000 × *g*, 10 min) and washing. All supernatants were collected for UV–vis analysis at the wavelength of 260 nm to quantify the LAP loading content.

Synthesis of CON3-LAP-HMON@GF7-ABS-PEG: 20 µL of EDC (120 mg mL^{-1}) and 20 µL of NHS (60 mg mL^{-1}) were added into the as-prepared CON3-LAP-HMON@GF7 solution (4.0 mL), and the mixture was kept under magnetic stirring for 30 min. After that, 40 µL of ABS stock solution (130 mg mL^{-1}) was added to the above mixture and reacted for 24 h. After the EDC/NHS-mediated covalent reaction, the solid products were collected by centrifugation and washing with ethanol three times.

PEGylation was subsequently utilized for surface modification. The obtained CON3-LAP-HMON@GF7-ABS was dissolved in $PEG-NH_2$ solution (4.0 mL, 2.0 mg mL^{-1}), and the mixture was kept under stirring for 12 h. After that, the solution was centrifuged (20 000 × *g*, 10 min) and rinsed by MilliQ water two times to obtain CON3-LAP-HMON@GF7-ABS-PEG.

Meanwhile, the CON3-HMON@GF7-PEG and CON3-LAP-HMON@GF7-PEG were synthesized using a similar procedure.

Supporting Information

Supporting Information is available from the Wiley Online Library or from the author.

Acknowledgements

This work was financially supported by Guangdong Provincial Natural Science Foundation of China (2021A1515010605), National Natural Science Foundation of China (32271374), Guangzhou Key Research and Development Program of China (202103000094), and Zhejiang Provincial Natural Science Foundation of China (LR19E030001). All animal procedures were performed in accordance with the Guidelines for Care and Use of Laboratory Animals of Southern Medical University, and approved by the Animal Ethics Committee of Southern Medical University. The assigned approval/accreditation number is SCXK(YUE)2021-0041.

Conflict of Interest

The authors declare no conflict of interest.

Data Availability Statement

The data that support the findings of this study are available from the corresponding author upon reasonable request.

Keywords

Fenton reaction cycloacceleration, high-performance ferroptosis therapy, hollow mesoporous organosilica nanoparticles, remodeling of tumor microenvironments, T_1-weighted magnetic resonance imaging

Received: December 27, 2022
Revised: February 21, 2023
Published online: March 17, 2023

---

[1] a) G. Lei, L. Zhuang, B. Gan, *Nat. Rev. Cancer* **2022**, *22*, 381; b) X. Jiang, B. R. Stockwell, M. Conrad, *Nat. Rev. Mol. Cell Biol.* **2021**, *22*, 266; c) S. Wu, C. Mao, L. Kondiparthi, M. V. Poyurovsky, K. Olszewski, B. Gan, *Proc. Natl. Acad. Sci. U. S. A.* **2022**, *119*, 2121987119; d) C. Wu, Z. Liu, Z. Chen, D. Xu, L. Chen, H. Lin, J. Shi, *Sci. Adv.* **2021**, *7*, 8833; e) H. Lee, F. Zandkarimi, Y. Zhang, J. K. Meena, J. Kim, L. Zhuang, S. Tyagi, L. Ma, T. F. Westbrook, G. R. Steinberg, *Nat. Cell Biol.* **2020**, *22*, 225.

[2] a) S. Zhang, L. Jin, J. Liu, Y. Wang, T. Zhang, Y. Liu, Y. Zhao, N. Yin, R. Niu, D. Xue, Y. Yu, Y. Yang, *Adv. Funct. Mater.* **2022**, *32*, 2113397; b) H. Liang, X. Wu, G. Zhao, K. Feng, K. Ni, X. Sun, *J. Am. Chem. Soc.* **2021**, *143*, 15812; c) B. Liu, Y. Bian, S. Liang, M. Yuan, S. Dong, F. He, S. Gai, P. Yang, Z. Cheng, J. Lin, *ACS Nano* **2021**, *16*, 617.

[3] a) S. Y. Peng, X. H. Liu, Q. W. Chen, Y. J. Yu, M. D. Liu, X. Z. Zhang, *Biomaterials* **2022**, *281*, 121358; b) G. Guan, C. Zhang, H. Liu, Y. Wang, Z. Dong, C. Lu, B. Nan, R. Yue, X. Yin, X. B. Zhang, G. Song, *Angew. Chem., Int. Ed.* **2022**, *61*, 202117229; c) D. W. Zheng, Q. Lei, J. Y. Zhu, J. X. Fan, C. X. Li, C. Li, Z. Xu, S. X. Cheng, X. Z. Zhang, *Nano Lett.* **2017**, *17*, 284.

[4] a) K. Li, C. Lin, M. Li, K. Xu, Y. He, Y. Mao, L. Lu, W. Geng, X. Li, Z. Luo, K. Cai, *ACS Nano* **2022**, *16*, 2381; b) C. C. Xue, M. H. Li, Y. Zhao, J. Zhou, Y. Hu, K. Y. Cai, Y. Zhao, S. H. Yu, Z. Luo, *Sci. Adv.* **2020**, *6*, 1346; c) S. Gao, H. Lin, H. Zhang, H. Yao, Y. Chen, J. Shi, *Adv. Sci.* **2019**, *6*, 1801733; d) P. Wang, M. Li, F. Zhou, Y. Yang, X. Yin, X. B. Zhang, G. Song, *Chem. Commun.* **2022**, *58*, 11107; e) L. Lei, Z. Dong, L. Xu, F. Yang, B. Yin, Y. Wang, R. Yue, G. Guan, J. Xu, G. Song, *Theranostics* **2022**, *12*, 6207.

[5] Z. Dong, P. Liang, G. Guan, B. Yin, Y. Wang, R. Yue, X. Zhang, G. Song, *Angew. Chem., Int. Ed.* **2022**, *61*, 202206074.

[6] R. Yue, C. Zhang, L. Xu, Y. Wang, G. Guan, L. Lei, X. Zhang, G. Song, *Chem* **2022**, *8*, 1956.

[7] M. Chang, Z. Hou, M. Wang, C. Yang, R. Wang, F. Li, D. Liu, T. Peng, C. Li, J. Lin, *Angew. Chem., Int. Ed.* **2021**, *60*, 12971.

[8] a) L. H. Fu, Y. Wan, C. Qi, J. He, C. Li, C. Yang, H. Xu, J. Lin, P. Huang, *Adv. Mater.* **2021**, *33*, 2006892; b) H. R. Burachaloo, P. A. Gurr, D. E. Dunstan, G. G. Qiao, *ACS Nano* **2018**, *12*, 11819.

[9] S. Koo, O. K. Park, J. Kim, S. I. Han, T. Y. Yoo, N. Lee, Y. G. Kim, H. Kim, C. Lim, J. S. Bae, J. Yoo, D. Kim, S. H. Choi, T. Hyeon, *ACS Nano* **2022**, *16*, 2535.

[10] J. E. Cun, Y. Pan, Z. Zhang, Y. Lu, J. Li, Q. Pan, W. Gao, K. Luo, B. He, Y. Pu, *Biomaterials* **2022**, *287*, 121687.

[11] a) P. Huang, X. Qian, Y. Chen, L. Yu, H. Lin, L. Wang, Y. Zhu, J. Shi, *J. Am. Chem. Soc.* **2017**, *139*, 1275; b) L. Li, Z. Yang, W. Fan, L. He, C. Cui, J. Zou, W. Tang, O. Jacobson, Z. Wang, G. Niu, S. Hu, X. Chen, *Adv. Funct. Mater.* **2020**, *30*, 1907716; c) Y. Guo, Y. Xu, Q. Bao, C. Shen, D. Ni, P. Hu, J. Shi, *ACS Nano* **2021**, *15*, 16286.

[12] Y. Ma, Z. Su, L. Zhou, L. He, Z. Hou, J. Zou, Y. Cai, D. Chang, J. Xie, C. Zhu, W. Fan, X. Chen, S. Ju, *Adv. Mater.* **2022**, *34*, 2107560.

[13] a) S. C. Chafe, F. S. Vizeacoumar, G. Venkateswaran, O. Nemirovsky, S. Awrey, W. S. Brown, P. C. McDonald, F. Carta, A. Metcalfe, J. M. Karasinska, L. Huang, S. K. Muthuswamy, D. F. Schaeffer, D. J. Renouf, C. T. Supuran, F. J. Vizeacoumar, S. Dedhar, *Sci. Adv.* **2021**, *7*, 0364; b) S. H. Lee, J. R. Griffiths, *Cancers* **2020**, *12*, 1616; c) Y. Lou, P. C. McDonald, A. Oloumi, S. Chia, C. Ostlund, A. Ahmadi, A. Kyle, S. Leung, D. Huntsman, B. Clarke, *Cancer Res.* **2011**, *71*, 3364; d) Q. Cao, D. J. Zhou, Z. Y. Pan, G. G. Yang, H. Zhang, L. N. Ji, Z. W. Mao, *Angew. Chem., Int. Ed.* **2020**, *59*, 18556.

[14] a) W. Zuo, W. Chen, J. Liu, S. Huang, L. Chen, Q. Liu, N. Liu, Q. Jin, Y. Li, P. Wang, X. Zhu, *ACS Appl. Mater. Interfaces* **2022**, *14*, 5053; b) Y. Zhou, S. Fan, L. Feng, X. Huang, X. Chen, *Adv. Mater.* **2021**, *33*, 2104223.

[15] X. Su, W. J. Wang, Q. Cao, H. Zhang, B. Liu, Y. Ling, X. Zhou, Z. W. Mao, *Angew. Chem., Int. Ed.* **2022**, *61*, 202115800.

[16] a) E. B. Guilmain, J. A. Menard, E. Lindqvist, V. I. Chandran, H. C. Christianson, M. C. Magana, J. Lidfeldt, G. M. Varga, C. Welinder, M. Belting, *Nat. Commun.* **2016**, *7*, 11371; b) H. S. Jung, J. Han, H. Shi, S. Koo, H. Singh, H. J. Kim, J. L. Sessler, J. Y. Lee, J. H. Kim, J. S. Kim, *J. Am. Chem. Soc.* **2017**, *139*, 7595; c) J. Li, K. Shi, Z. F. Sabet, W. Fu, H. Zhou, S. Xu, T. Liu, M. You, M. Cao, M. Xu, X. Cui, B. Hu, Y. Liu, C. Chen, *Sci. Adv.* **2019**, *5*, 0937.

[17] X. Chen, H. Zhang, M. Zhang, P. Zhao, R. Song, T. Gong, Y. Liu, X. He, K. Zhao, W. Bu, *Adv. Funct. Mater.* **2019**, *30*, 1908365.

[18] L. Shi, Y. Wang, C. Zhang, Y. Zhao, C. Lu, B. Yin, Y. Yang, X. Gong, L. Teng, Y. Liu, X. Zhang, G. Song, *Angew. Chem., Int. Ed.* **2021**, *60*, 9562.

[19] a) S. Wang, G. Yu, Z. Wang, O. Jacobson, L. S. Lin, W. Yang, H. Deng, Z. He, Y. Liu, Z. Y. Chen, X. Chen, *Angew. Chem., Int. Ed.* **2019**, *58*, 14758; b) M. Ye, Y. Han, J. Tang, Y. Piao, X. Liu, Z. Zhou, J. Gao, J. Rao, Y. Shen, *Adv. Mater.* **2017**, *29*, 1702342.

[20] a) H. Zhou, X. Lu, C. Du, Z. Zhou, J. Feng, Z. Liang, Y. Xu, X. Qiu, Z. Shen, *Small* **2022**, *18*, 2202705; b) S. Guo, Z. Li, J. Feng, W. Xiong, J. Yang, X. Lu, S. Yang, Y. Xu, A. Wu, Z. Shen, *Nano Today* **2022**, *47*, 101663.

[21] L. Huang, Y. Lu, S. Guo, J. Yang, Z. Liang, Q. Zhang, P. Yi, Y. Feng, Y. Li, Y. Xu, Z. Shen, *Adv. Funct. Mater.* **2023**, *33*, 2209278.